Journal of Biomedical Optics

SPIEDigitalLibrary.org/jbo

Oblique incidence reflectometry: optical models and measurements using a side-viewing gradient index lens-based endoscopic imaging system

R. Andrew Wall
Jennifer K. Barton

SPIE

Oblique incidence reflectometry: optical models and measurements using a side-viewing gradient index lens-based endoscopic imaging system

R. Andrew Wall[a] and Jennifer K. Barton[a,b,*]
[a]University of Arizona, College of Optical Sciences, 1630 E. University Boulevard, Tucson, Arizona 85721
[b]University of Arizona, Department of Biomedical Engineering, 1127 E. James E. Rogers Way, Tucson, Arizona 85721

Abstract. A side-viewing, 2.3-mm diameter oblique incidence reflectometry endoscope has been designed to obtain optical property measurements of turbid samples. Light from a single-mode fiber is relayed obliquely onto the tissue with a gradient index lens-based distal optics assembly and the resulting diffuse reflectance profile is imaged and collected with a 30,000 element, 0.72 mm clear aperture fiber bundle. Sampling the diffuse reflectance in two-dimensions allows for fitting of the reflected intensity profile to a well-known theoretical model, permitting the extraction of both absorption and reduced scattering coefficients of the tissue sample. Models and measurements of the endoscopic imaging system are presented in tissue phantoms and *in vivo* mouse colon, verifying the endoscope's capabilities to accurately measure effective attenuation coefficient and differentiate diseased from normal colon. [DOI: 10.1117/1.JBO.19.6.067002]

Keywords: oblique incidence reflectometry; tissue optical properties; absorption coefficient; reduced scattering coefficient; endoscope; gradient-index; gastrointestinal; colon.

Paper 130601R received Aug. 18, 2013; revised manuscript received Apr. 7, 2014; accepted for publication May 1, 2014; published online Jun. 3, 2014.

1 Introduction

Accurate measurements of the optical properties of a tissue enhance the ability to monitor tissue metabolic status or diagnose disease.[1–3] Changes in the absorption coefficient, μ_a, and reduced scattering coefficient, $\mu_s' = \mu_s(1-g)$, where μ_s is the scattering coefficient and g is the scattering anisotropy, have been related to critical anatomical markers of various diseases.[4–8] These findings have led to studies that have shown efficient differentiations of malignant and benign tissues by measuring tissue optical properties.[9–11]

The most common method of evaluating tissue properties is through integrating sphere measurements,[12] though this setup is usually limited to thin *ex vivo* tissue samples. Through implementation of diffusion theory, which is valid for observation points far from the light source, optical fiber bundles[13] and video reflectometers[14] have been used to measures a tissue's diffuse reflectance profile and compute optical properties. These single wavelength implementations utilized a normally incident light source and either measured only the effective attenuation coefficient, μ_{eff}, or assumed absorption in the tissue to be negligible while measuring only μ_s'.

In order to decompose the effective attenuation into its subcomponents, a second measurement needs to be taken. Introducing non-normal illumination, i.e., changing the incoming source angle, effectively shifts the center of the diffuse reflectance profile as per Snell's law and the tissue's optical properties.[15] Measurement of this offset in addition to the falloff of the diffuse reflectance profile by oblique incidence reflectometry (OIR) allows for the extraction of not only effective attenuation, but also its separation into absorption and scattering components. This method has been demonstrated in optical fiber-based probes.[16] Spectrally resolved OIR measurements, also called oblique incidence diffuse reflectance spectroscopy (OIDRS), can be made with the introduction of a broadband source and a spectrometer, providing the calculation of optical properties at multiple wavelengths.[17] Recently, OIDRS has been used for minimally invasive tumor margin detection[18] and epithelial cancer detection,[19] and has been combined with confocal microscopy for increased capability as a diagnostic tool.[20]

There exist other *in vivo* methods of extracting tissue optical properties. For example, optical coherence tomography (OCT) has been utilized for this purpose.[21–23] OCT utilizes singly backscattered photons as opposed to diffuse scattering photons.[24–26] Due to the confounding effects of speckle, averaging of multiple depth scans is necessary for accurate estimates, and only an effective backscattering coefficient can be measured. Elastic scattering spectroscopy (ESS),[27,28] phase contrast microscopy,[29] near-infrared diffuse optical tomography,[30] and spatial-frequency domain imaging using modulated illumination[31] have also been used to extract tissue optical properties, but their complex imaging geometries preclude their use in endoscopes small enough for use in minute luminal structures such as the mouse colon.

For this purpose, a side-viewing OIR endoscope is needed that is ~2 mm in diameter. Conventional OIR and OIDRS probes use a source fiber to obliquely illuminate the sample, and place a few sampling fibers on either side of the source fiber at interval distances.[16,32] These probes require tissue surface contact and can be relatively large in size, the smallest on the order of 4 to 5 mm.[18] OIR probes are also usually forward-looking, although recent systems have utilized waveguides[19] and unfocused reflective optics[4] to collect diffuse reflectance

*Address all correspondence to: Jennifer K. Barton, E-mail: barton@u.arizona.edu

from the side. Other probes for use in optical tissue characterization have been presented but they, too, are usually larger than 2.5 mm in diameter or utilize spectroscopic proximal setups that require fewer distal fibers.[33–35] We have constructed a 2.3-mm diameter gradient index (GRIN) lens and right-angle prism-based endoscope that obliquely illuminates the surface of the target tissue with a single wavelength of light and images the diffuse reflectance onto a 30,000 element fiber bundle, which relays light to a proximal setup for signal collection and processing. In this paper, we describe our models and methods for developing this OIR diagnostic tool.

2 Materials and Methods

2.1 *OIR Theory*

A complete description of OIR theory can be found in Lin et al.,[16] and a summary of relevant equations are given below. Photons incident upon biological tissue or turbid media propagate a probabilistic distance before they are scattered or absorbed. This average distance, one mean free path (mfp′) from the point of incidence along the direction of light propagation, is related to the diffusion constant, D, as determined by the absorption and scattering coefficients of the tissue:

$$1\ \text{mfp}' \sim 3D = \frac{1}{C\mu_a + \mu_s'}, \tag{1}$$

where the constant C is estimated to be between 0.35 and 1.[15] For a system with illumination incident into the tissue at an angle, θ_t (Fig. 1), photons travel to an average depth, 3D cos θ_t, below the surface before an interaction event. Following the work by Farrell and Wang[36,37] on the lumped positive- and negative-source interaction approximation of diffusion theory, a profile can be fit to diffuse reflected light escaping the tissue's two-dimensional (2-D) surface and collected at distances $r > 1$ mfp′, away from the peak:[16]

$$R(r,0) = 3D\cos\theta_t\left(\mu_{\text{eff}} + \frac{1}{\rho_1}\right)\frac{\exp(-\rho_1\mu_{\text{eff}})}{\rho_1^2} + (3D\cos\theta_t + 4\text{D}) \times \left(\mu_{\text{eff}} + \frac{1}{\rho_2}\right)\frac{\exp(-\rho_2\mu_{\text{eff}})}{\rho_2^2}, \tag{2}$$

where ρ_1 and ρ_2 are the distances from the negative and positive sources, respectively, to a point $(r, 0)$ on the tissue's surface. Fitting a profile to the scaled diffuse reflectance profile, $kR(r,0)$, yields values for the shift in the profile peak, Δr, as a consequence of oblique illumination and μ_{eff}, allowing for the extraction of absorption and scattering coefficients:

$$\mu_a = \frac{\mu_{\text{eff}}^2 \Delta r}{3C\ \sin\ \theta_t}, \tag{3}$$

$$\mu_s' = \frac{\sin\ \theta_t}{\Delta r} - C\mu_a. \tag{4}$$

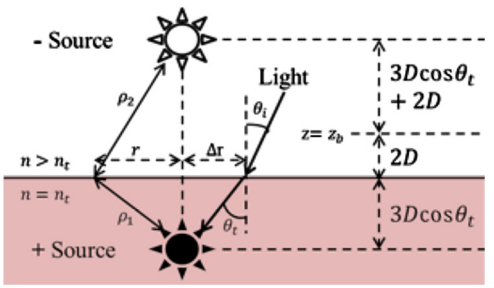

Fig. 1 For a non-normally incident source, photons travel an average distance, three-dimensional, at a refracted angle, θ_t, before they are scattered. The peak of the diffuse reflectance profile is shifted by some distance, Δr, and can be sampled at various distances, r, away from the peak, after which Eq. (2) can be fit to the profile.

2.2 *Optical System Design*

The OIR system was inspired by a dual-modality surface magnifying chromoendoscopy (SMC)–OCT endoscopic system built in our laboratory, which was previously described in detail.[38] This system simultaneously collected surface images and cross-sectional OCT images of the mouse colon. Due to the OCT channel being axially asymmetric, the OCT beam had non-normal incidence on the tissue. Analysis of the design suggested that with modifications, the system could be used for OIR. A description of the system is described in the following sections.

2.2.1 *Proximal system design*

A fiber-coupled laser diode with an illumination wavelength, $\lambda = 638$ nm (Fibertec II, Blue Sky Research, Milpitas, California), was coupled directly into a single-mode fiber which fed into the endoscope and illuminated the sample. Diffuse reflected light collected by distal endoscope optics from the sample's surface was relayed with a 30,000 element, 0.72 mm clear aperture fiber bundle (IGN-08/30, Sumitomo Electric USA, Torrance, California). The proximal face of the fiber was imaged onto a charge-coupled device (CCD) array (PIXIS 1024, Princeton Instruments, Trenton, New Jersey) with a 20× microscope objective (PLN 20×, Olympus America, Center Valley, Pennsylvania) and a simple 60 mm focal length achromatic doublet. The proximal fiber bundle face was imaged to approximately 60% of the area of the 1 megapixel CCD, and a computer read out data. At a laser power of 2.5 mW on the sample, OIR images were acquired with integration times of 20 ms with a readout time of 420 ms.

2.2.2 *Endoscope design*

The fiber bundle was attached to a custom spacer and GRIN lens-based distal optics assembly to provide 1:1 magnification at an air-equivalent working distance of 1.58 mm. An aluminized right-angle prism was attached to the distal face of the GRIN lens to enable side-viewing, and the assembly was protected by insertion into a glass envelope with an inner diameter of 1.9 mm and outer diameter of 2.3 mm. The GRIN lens and spacer had diameters of 1.8 mm, compared to the 0.72 mm clear aperture of the fiber bundle, which prevented vignetting of the source or diffusely reflected light. A 0.7 mm clear aperture stop was added between the GRIN lens and right-angle prism to decrease the size of the GRIN lens entrance pupil and avoid possible total internal reflection of diffusely reflected light at the circumference of the GRIN lens, and reduce signal contamination from light collected by the prism from outside the desired tissue inspection area. The resulting system was capable of

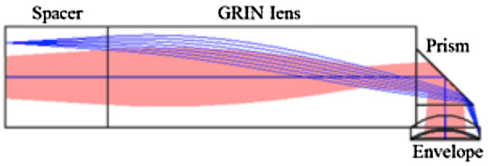

Fig. 2 Optical model of oblique incidence reflectometry (OIR) illumination and collection. The source fiber is moved to a position resulting in 638 nm incident illumination (dark gray, blue online) at 18 deg away from the fiber bundle imaging field-of-view (light gray, pink online) and focused 30 μm inside the tissue with an NA = 0.14.

resolving 100 to 125 lp/mm features across a 0.70 mm field-of-view.

One 780-HP (Nufern, East Granby, Connecticut) single-mode fiber with a numerical aperture (NA) of 0.13 was placed at the 12:00 position with respect to the right-angle prism at an off-axis radial distance of 0.6 mm. This fiber placement resulted in an unvignetted source beam that refracted into the tissue, at an angle of 18 deg away from, and a distance of 600 μm outside the edge of, the fiber bundle imaging field-of-view. The beam focus was 30 μm inside the tissue with a weak NA of 0.13 (Fig. 2).

2.2.3 *Mechanical design*

A custom ferrule was designed with an outer diameter equal to that of the spacer and GRIN lens to ease alignment, with holes bored to hold the source fiber ($d = 125$ μm) and the imaging fiber bundle ($d = 800$ μm) in their correct relative orientation and spacings (Fig. 3). The ferrule also had holes bored to accommodate single-mode fibers ($d = 125$ μm) at 1:30, 4:30, 7:30, and 10:30 positions around the circumference of the fiber bundle for the added capability of other imaging modalities such as OCT if desired. For ease of construction, ferrules were fabricated with a proximal lead-in. Elements were secured together with a UV curing epoxy (Norland 63, Norland Products, Cranbury, New Jersey) which offered high transmission for $\lambda = 638$ nm. Proximal to the ferrule, fibers were protected with polyimide tubing with an inner diameter of 1.45 mm and a wall thickness of 57 μm (B0013H0X8E, SmallParts, Seattle, Washington). The full assembly was inserted into an outer sheath consisting of a 1.9-mm inner diameter, 2.3-mm outer diameter glass envelope fixed to polyimide tubing with an inner diameter of 2.23 mm and a similar wall thickness

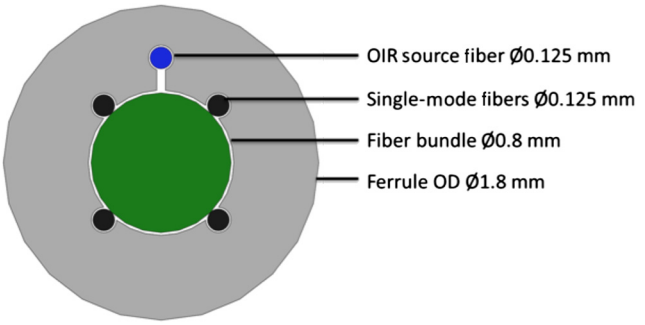

Fig. 3 Drawing of the distal face of the fiber ferrule. The OIR source fiber is located at the 12:00 position at a center-to-center spacing from the central fiber bundle of 0.6 mm. Four single-mode fibers (placed around the circumference of the fiber bundle allow for the possibility of other imaging modalities such as optical coherence tomography (OCT).

(B0013HR0I4) using a short polyimide tube collar with an inner diameter of about 2.3 mm.

2.3 *Adaptation of OIR Theory to Existing Endoscope*

The existing endoscope was unique compared to the conventional tools that measure diffuse reflectance. The model described above is valid for measurements made at the surface of a flat sample at a distance greater than 1 mfp′ from the source. Our system, however, imaged the asymmetric diffuse reflectance from a cylindrical sample that was illuminated with a nonzero NA beam. With a cylindrical sample, light had to travel further to escape the tissue toward the edge of the field-of-view in the azimuthal direction. Aberrations introduced by real optical components also changed the shape of the diffuse reflectance profile collected by the fiber bundle. Furthermore, previously published OIR systems measured the shift in the diffuse reflectance profile by analyzing the intensity of the light coming back on either side of the source fiber. Measurements were taken both in front (positive measurements) and behind (negative measurements) the angle of incidence at equal distances from the source, and $\Delta r = 0$ theoretically resulted in both measurements yielding an equal intensity. In our design, we were only sampling negative measurements. Therefore, if measurements were taken only along the plane of incidence it would be impossible to tell the position of the profile's peak. However, collecting 2-D data with a fiber bundle allowed for alternative methods to be used for the calculations of Δr and μ_{eff}.

The location of the diffuse reflectance peak was extrapolated from the 2-D data using image gradients. The imgradient operator was used in MATLAB (MathWorks, Natick, Massachusetts) resulting in gradients calculated for each pixel of some direction and magnitude. To exclude points most affected by the cylindrical curvature, points beyond one-half the radius of the imaged area in the azimuthal direction were excluded from the peak extrapolation (Fig. 4). Once the center of the reflectance profile was estimated, Δr could be calculated by subtracting the known incident illumination point.

A different mask was applied to the imaged area to select a region appropriate for fitting to $kR(r, 0)$. Measurements inside of a circular mask of radius 0.6 mm with the origin located at the incident illumination point (half of the diameter and approximately 1/3 of the area of the fiber bundle) were excluded (Fig. 4). This radius was chosen based on expected colon tissue optical properties and the limitation of Eq. (2) above only being valid more than 1 mfp′ away from the illumination source. A 2-D surface profile was taken, and the robust fitting of $kR(r, 0)$ to the smoothed data using a Levenberg–Marquardt least-squares fit enabled the extraction of μ_{eff}.

To assess the OIR capabilities of the endoscope and the suitability of this adapted theory, we performed four experiments. First, we modeled our endoscope using a nonsequential ray-tracing program, which could also simulate absorption and volume scatter in a sample. Second, tissue phantoms were fabricated and imaged with a bare fiber bundle spaced 0.8 mm away from a fiber that provided obliquely incident illumination at 30 deg away from the fiber bundle. This experiment enabled us to confirm that collecting 2-D data allowed for the calculation of Δr without both positive and negative measurements. It also allowed for the fitting of $kR(r, 0)$ to a dataset without aberrations caused by the spacer-GRIN lens-prism-envelop optics assembly. Third, we imaged these same tissue phantoms with

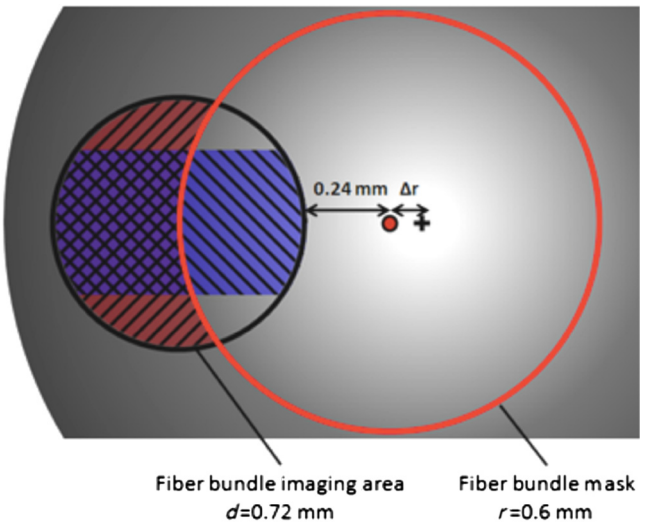

Fig. 4 Top-down illumination-imaging geometry for the OIR endoscope. Light incident on the tissue (gray dot, red online) refracts into the turbid media, and results in a diffuse reflectance profile centered (black cross) some distance, Δr, away. Diffuse reflectance imaged onto the middle 50% of the fiber bundle (left diagonals, shaded blue online) was used to calculate Δr, after which the fiber area was masked with a circular mask (gray circle, red online) of radius 0.6 mm, centered at the point of incident illumination. The resulting fiber area (right diagonals, shaded red online) was used to extract μ_{eff}.

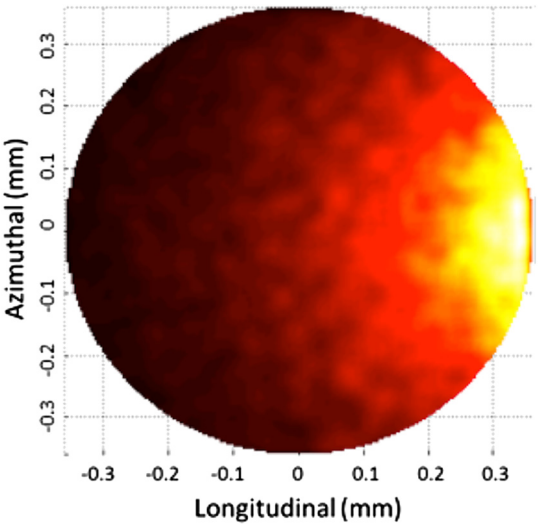

Fig. 5 Simulated FRED analysis plot of diffuse reflectance from a tissue ($\mu_a = 1$ mm^{-1}, $\mu_s' = 2.5$ mm^{-1}, $g = 0.9$) shows irradiance collected by fiber bundle in both longitudinal and azimuthal directions.

a fully constructed OIR endoscope. Fourth, we demonstrated the endoscope's capabilities for imaging in the *in vivo* mouse colon.

2.3.1 *Modeling of OIR endoscope*

The distal endoscope optics assembly was modeled in FRED (Photon Engineering, Tucson, Arizona) to assess the endoscope's OIR capabilities. Light propagated through the system and illuminated a semi-infinite tissue model with refractive index, $n = 1.4$, and cylindrical surface in contact with the endoscope envelope. A range of tissue absorption and reduced scattering properties spanning those reported in the literature for colon[39–43] were used: μ_a, between 0.125 and 1 mm^{-1} and μ_s' between 0.25 and 2.5 mm^{-1}, with g constant at 0.9. Diffuse light remitted from the tissue, imaged back through the distal optics, and collected within the NA of the fiber bundle was studied at an analysis surface whose square dimension was the same diameter as the clear aperture of the fiber bundle, CA = 0.72 mm, and whose bin size was equal to the core size of a single fiber element within the bundle (Fig. 5). The 2-D data were smoothed with a moving average filter with an 8×8 kernel size and masked to the circular fiber bundle imaging area. Simulation was performed in nonsequential ray trace mode with 10 million rays, the practical limit for a desktop machine. Due to the low probability of capturing a launched ray, simulated data were noisier than experimentally obtained images. The calculations described above were then used to determine Δr, μ_{eff}, μ_a, and μ_s' for each simulated tissue.

2.3.2 *Tissue phantoms*

Tissue phantom preparation. Methylene blue (M291, Thermo Fisher Scientific, Waltham, Massachusetts) and 0.76-μm diameter polystyrene beads (PS03N, Bangs Laboratories, Fishers, Indiana) were used to supply absorption and scattering in our tissue phantoms. Using the molar extinction coefficient and molecular weight of methylene blue, and a Mie scattering calculator[44] to determine needed concentrations, a matrix of 2-D serial dilutions was used to fabricate samples with the optical properties $\mu_a = 0.125$, 0.25, 0.5, 0.75, and 1 mm^{-1}, $\mu_s' = 0.25$, 0.5, 1.0, 1.5, 2.0, and 2.5 mm^{-1}, and $g = 0.9$, resulting in 30 different tissue phantoms.

Tissue phantom imaging and processing. Images of each tissue phantom were taken with both the bare fiber bundle/oblique incidence illumination fiber setup, and the full OIR-configured endoscope. For both systems, calibration images with the distal optics immersed in water with the source and room lights off were taken to calculate CCD dark noise. The source was then turned on and images were taken of background signal, including reflections at optical interfaces. Finally, a concave surface coated with Spectralon (Labsphere, North Sutton, New Hampshire) was imaged to simulate a uniform Lambertian reflector to estimate spatial transmission ambiguities across the fiber bundle face (e.g., dark pixels). Dark noise and background signal were subtracted from images, after which they were divided by the spatial system response. Images were subsequently median filtered with a 9×9 kernel to reduce impulsive noise, then filtered with a Gaussian low-pass filter with a kernel size approximately equal to two times the core-to-core spacing of the fiber bundle to remove fiber bundle pixilation, as previously described in detail.[45] Filtered images were processed as described above, with image gradients used to triangulate the location of the diffuse reflectance peak and masked imaged profiles fit to Eq. (2). Fits of Δr and μ_{eff} enabled the extraction of an experimental μ_a and μ_s' for each tissue phantom using Eqs. (3) and (4).

2.3.3 *Animal imaging*

All studies were performed in accordance with a University of Arizona Institutional Animal Care and Use Committee approved

protocol. One A/J mouse treated with the colon-specific carcinogen azoxymethane (10 mg/kg, weekly injections for five weeks) was imaged to provide-proof-of-concept of the operation and diagnostic use of the OIR endoscope. Twenty-four hours prior to imaging, the mouse was fasted and given Pedialyte in place of water to clear the colon. Immediately prior to imaging, the mouse was anesthetized with a mixture of Ketamine (0.33 mg/ml, 100 mg/kg) and Xylazine (0.033 mg/ml, 10 mg/kg) administered IP. The colon was gently flushed with 3 to 9 ml of warm saline to clear excess mucous. The endoscope was coated with a thin layer of biocompatible water-based lubricant and inserted approximately 32 mm inside the colon. OIR measurements were made of the ventral colon at 0.18 mm increments, half of the longitudinal measurement range, resulting in 168 measurements along the 30 mm of mouse colon. After OIR data collection, an OCT image of the same rotation was taken to coregister extracted tissue optical properties with morphological tissue information.

3 Results

3.1 *Optical Simulations*

Thirty tissues were simulated with the same optical properties as the experimental phantoms. Using FRED analysis tools, irradiance plots were obtained at the analysis surfaces in the full OIR endoscope models, the offset and effective attenuation coefficients extracted, and the absorption and reduced scattering coefficients computed. When only tissue phantoms with a μ_{eff} within the design limits of the OIR system were considered, the average error in the extracted effective attenuation coefficient and location of the peak diffuse reflectance was 5% and 12% of the expected values with a standard deviation of 8% and 5%, respectively. The maximum error was 32% and 20%, respectively (Fig. 6). Using these values, calculated absorption coefficients were obtained with a more significant error (75% average, 145% maximum). Calculated absorption and reduced scattering coefficients showed only a weak correlation with true values.

3.2 *Tissue Phantom Imaging*

Tissue phantoms were imaged with the bare fiber setup and OIR endoscope. Five of the 30 phantoms suffered from rapid precipitation and data could not be successfully collected. When the bare fiber bundle/oblique incidence source fiber arrangement was used (Fig. 7), the effective attenuation coefficients were measured to within an average of 4% of the expected values (12% standard deviation, 31% maximum error). The location of the peak diffuse reflectance was detected with an average of <2% error (1.3% standard deviation, 4.9% maximum error). μ_a and μ_s' were calculated with 14% average error (14% standard deviation, 52% maximum error), and 11% average error (10% standard deviation, 36% maximum), respectively. When using the OIR endoscope (Fig. 8), the results were slightly poorer than those obtained with the simulations, and considerably poorer than the bare fiber setup imaging results. The average error of the effective attenuation coefficients and locations of the diffuse reflectance peaks were within 10% and 15% of their respective expected values (15% and 14% standard deviation and 37% and 27% maximum error, respectively). Computed μ_a and μ_s' showed a weak correlation with true values.

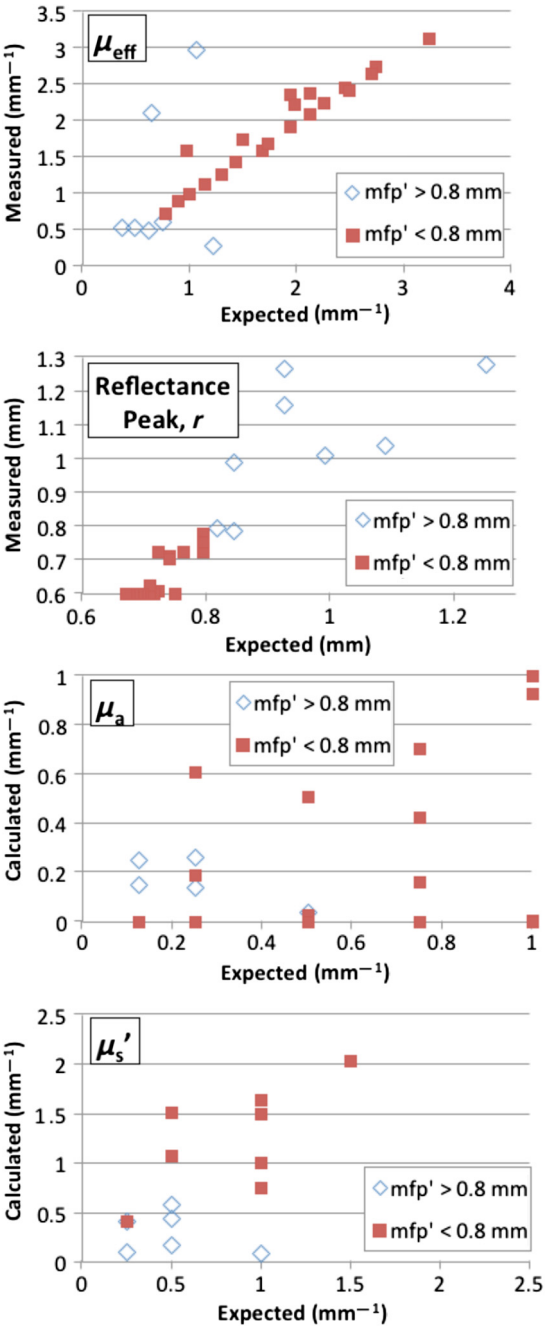

Fig. 6 Expected versus calculated effective attenuation coefficients (μ_{eff}), offsets, and absorption (μ_a) and reduced scattering coefficients (μ_s') for FRED-simulated tissue optical phantoms and the full OIR endoscope. Measurements of phantoms with mean free paths (mfp′) > 0.8 mm (outside design limits) are marked with diamonds, while measurements for those with an mfp′ < 0.8 mm are marked by squares.

3.3 *Animal Imaging*

Images were successfully obtained in the *in vivo* mouse colon with the OIR endoscope. After coregistering OIR calculations with OCT images (Fig. 9), healthy colon was measured to

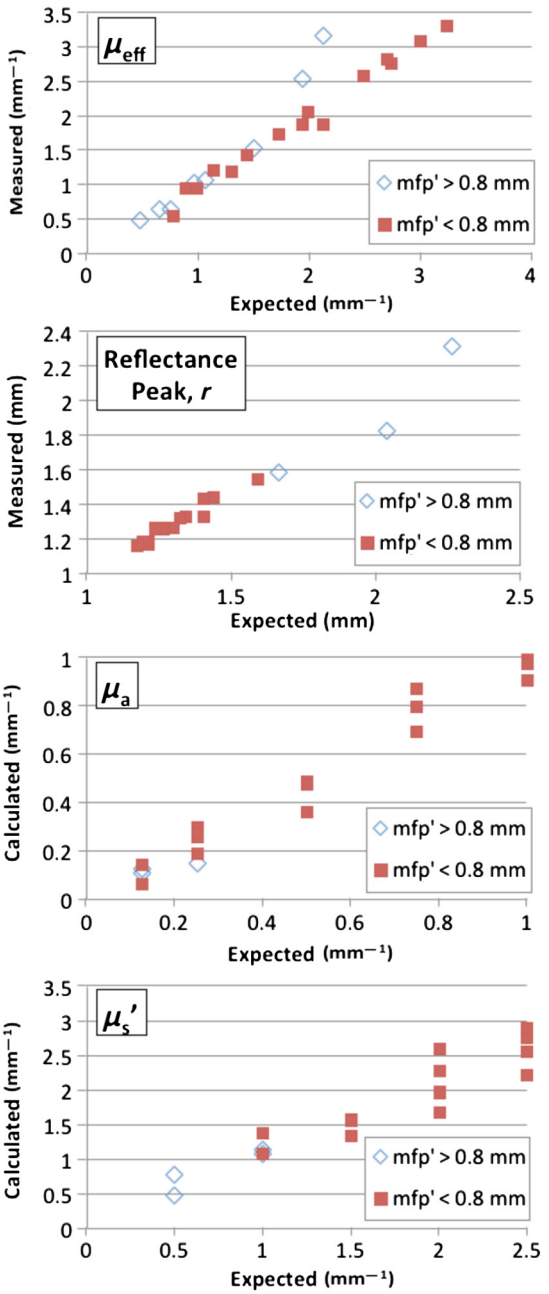

Fig. 7 Expected versus calculated effective attenuation coefficients (μ_{eff}) for tissue optical phantoms experimentally measured with the bare fiber bundle and obliquely incident fiber setup. Measurements of phantoms with mean free paths (mfp′) < 0.8 mm are marked with diamonds, while measurements for those with an mfp′ < 0.8 mm are marked by squares.

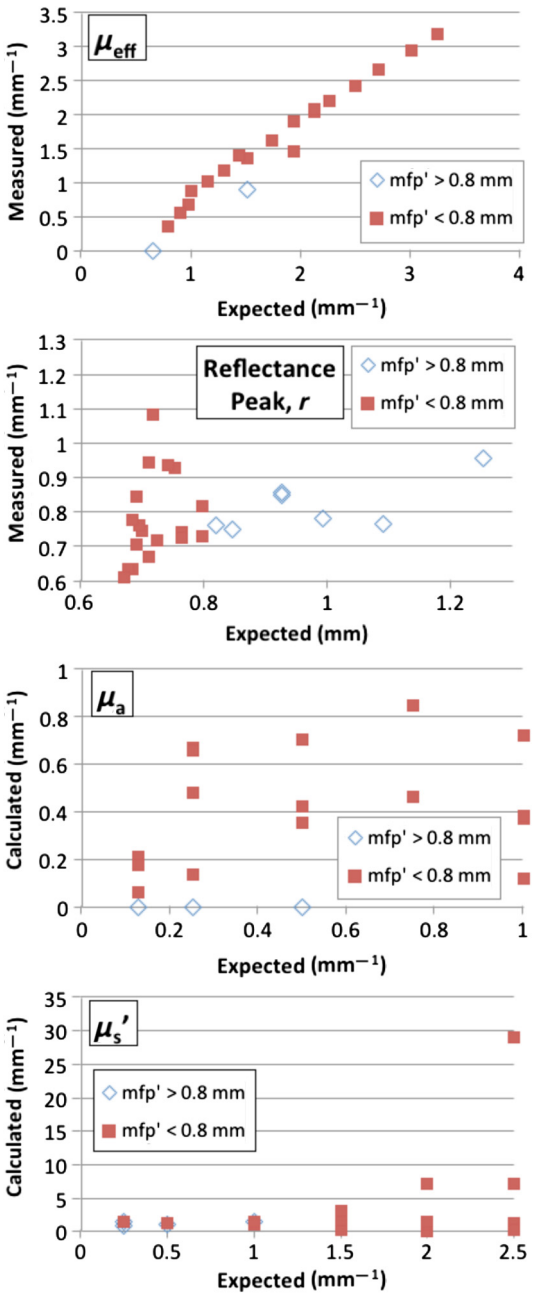

Fig. 8 Expected versus calculated offsets, effective attenuation coefficients (μ_{eff}), and absorption (μ_a) and reduced scattering coefficients (μ_s') for tissue optical phantoms experimentally measured with the full OIR endoscope. Measurements of phantoms with mean free paths (mfp′) < 0.8 mm are marked with blue diamonds, while measurements for those with an mfp′ < 0.8 are marked by red squares.

have an average $\mu_{eff} = 1.35\ mm^{-1}$, while adenoma was measured to have an average $\mu_{eff} = 2.15$.

4 Discussion

A small diameter endoscopic OIR system was designed and tested on modeled and fabricated tissue phantoms, and demonstrated in the *in vivo* mouse colon. The most unique aspect of this endoscope is the concept of using a 2-D fiber bundle to collect diffuse reflectance from only one (the negative) side of the angled incident illumination, and using image gradients to estimate the location of the diffuse reflectance peak. By

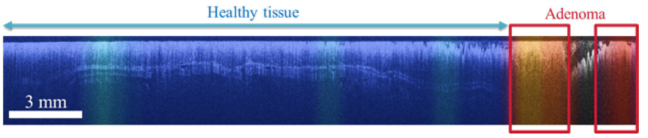

Fig. 9 Section of 30 mm *in vivo* mouse colon imaged with OCT and coregistered with OIR measurements. Image is colored with effective attenuation coefficients between 1.35 (blue) and 2.15 mm^{-1} (red).

avoiding the need for data collection on both sides of the angled incident illumination, very small endoscopes using conventional distal GRIN optics can be fabricated. All that is needed to create angled illumination is to place the illumination fiber off the central optical axis. Such endoscopes can be forward looking or side-looking with the addition of a right-angle prism or other reflecting surface. An advantage of this technique is that it requires the use of only one wavelength of illumination. Techniques like ESS or DRS can be used to measure spectrally resolved μ_a and μ_s', and might be packaged into a small endoscope. However, they require the use of multiple wavelengths, thus requiring multiplexed light sources or a white light source and monochrometer.[27,28,33,34,46] This OIR endoscope currently utilizes a high performance camera and large element fiber bundle, although the former is unnecessary and the latter might be replaced with a smaller element bundle to reduce costs. The incorporation of a fiber bundle in the endoscope could also enable multimodality usage, such as fluorescence imaging in addition to OIR.

The essential concept of this endoscope design was proven using a bare fiber probe. Good estimates of the effective attenuation coefficient were obtained, and the error in the measurement of the diffuse reflectance peak was very small (<2%), suggesting that the image gradient estimation method is appropriate and accurate. The bare fiber probe also showed the capability to decompose the absorption and reduced scattering coefficients when both the effective attenuation coefficient and the shift in the peak reflectance profile can be accurately measured. For both simulations and experiments using the full OIR endoscope, estimation of the effective attenuation coefficient was also good, though the accuracy of the diffuse reflectance peak location measurements was significantly degraded, which resulted in large errors in the calculated absorption and reduced scattering coefficients.

The reason for unsuccessful calculation of μ_a and μ_a' appears to be the high sensitivity of Eqs. (3) and (4) to errors in the estimation of the diffuse reflectance peak location. Although the average error in the measurement of the absolute peak location for the OIR endoscope experiments was a modest 15%, the error in Δr (the shift of the peak from the normally incident location) was greater (70% average). As evident from Eqs. (3) and (4), this error is compounded in the extraction of μ_a and μ_s', and as noted in the literature,[16] absorption coefficient calculations that rely on measuring Δr are more sensitive to error in OIR measurements. The cylindrical image plane and imaging aberrations induced by the GRIN-based distal optics, both of which caused rotational asymmetry about the peak of the imaged diffuse reflectance profile, are the most significant challenge and preclude the accurate calculation of Δr with the relatively simple method employed here. The cylindrical object plane causes light to be more highly attenuated at the azimuthal edges of the fiber bundle imaging area due to the added tissue thickness in those regions. For this reason, measurements at the azimuthal edges of the fiber bundle were excluded from the image gradient calculations. However, even the more central region utilized suffered from this error, and the exclusion of the edge measurement reduced the robustness of the gradient calculation. Additionally, field curvature and distortion in the GRIN-prism optical assembly, strongest along the longitudinal axis, caused reflected photons to be imaged to skewed positions on the fiber bundle. An image gradient method that incorporated the endoscope-specific optical aberrations and the curved sample surface would lead to better estimates. Since these sources of error are deterministic, they can be compensated for in the calculation of μ_a and μ_s'.

An alternative approach would be to correlate experimentally obtained images to a library of simulated results from tissues with varying optical properties. This latter method has been used successfully by Garcia-Uribe et al.[19] to deduce the absorption and scattering properties of a sample. The diffuse reflectance profile extracted from the optical model, unlike the diffusion-theory-based model proposed in Eq. (2), would be valid at all measurement points and would account for endoscope aberrations and sample geometries. Since no model is being fit, measurements inside 1 mfp′ may be utilized, and a wider range of tissue optical properties could be measured.

Regardless of the method utilized to extract tissue optical properties, careful endoscope design will maximize the accuracy of calculated results. This OIR endoscope was designed to optimize measurement capability while miniaturizing diameter. A challenge with a small diameter endoscope is the limited source–detector fiber separation and limited source illumination incidence angles that can be easily achieved. By moving the source fiber out radially in the endoscope, the source incidence position moves away from the fiber bundle detection area, maximizing the area that could be used to fit a profile to diffuse reflectance. In this endoscope, the source fiber was moved as far out as possible while avoiding vignetting in the distal optics (in this case, at the aluminized face of the right-angle prism). Incorporating a custom prism with a slightly larger edge width, or a rod prism with a diameter matching the GRIN lens, could enable about a 25% increase in center-to-center source separation. Further separation would result in loss of light or require a larger diameter endoscope. The clocking of the source fiber position not only changed the focal depth of the illumination spot, but also changed the angle of incident illumination angle between 10 deg toward and 18 deg away from the fiber bundle imaging area, with respect to the normal of the cylindrical envelope. For OIR, a larger angle of incidence leads to a larger Δr shift, which can be more robustly detected. We also desired the focus of the source to be just outside the window, which would be closest to the model assumption of a collimated source. The 12:00 clocking used in this design maximized the angle at 18 deg while keeping the focus 30 μm into the tissue. More complex optical geometries might also allow for a higher angle of oblique incidence, maximizing Δr, but will be challenging to package in a small diameter endoscope. Finally, the use of an even smaller NA fiber, more closely resembling a collimated beam as approximated by the diffusion theory would be helpful, although the 0.13 NA fiber utilized here is near the limit of commercially produced fibers.

Despite limitations of the current system, the small diameter OIR endoscope has proven to be useful, and experiments in the mouse colon were successful. The measured effective attenuation coefficient varied between visually normal and adenomatous tissue, and was increased in adenoma, in agreement with previously reported studies.[39–43] Further improvements in endoscope design and the method of extracting tissue optical properties (μ_a and μ_s') will enable additional future functionality.

Acknowledgments

Research reported in this paper was supported by the National Cancer Institute of the National Institutes of Health under Award No. R01 CA109385. The content is solely the responsibility of

the authors and does not necessarily represent the official views of the National Institutes of Health.

References

1. S. L. Jacques, Ed., *Laser–tissue interaction VIII*, *Proc. SPIE* **2975** (1997).
2. E. M. Sevick-Muraca and D. Benaron, Eds., *OSA Trends in Optics and Photonics on Biomedical Spectroscopy and Diagostics*, Vol. 3, Optical Society of America, Washington, DC (1996).
3. R. Chance and R. R. Alfano, Eds., *Optical Tomography and Spectroscopy of Tissue: Theory, Instrumentation, Model, and Human Studies II*, *Proc. SPIE* **2979** (1997).
4. P. R. Bargo et al., "In vivo determination of optical properties of normal and tumor tissue with white light reflectance and an empirical light transport model during endoscopy," *J. Biomed. Opt.* **10**(3), 034018 (2005).
5. T. C. Zhu, J. C. Finlay, and S. M. Hahn, "Determination of the distribution of light, optical properties, drug concentration, and tissue oxygenation in-vivo in human prostate during motexafin lutetium-mediated photodynamic therapy," *J. Photochem. Photobiol. B* **79**(3), 231–241 (2005).
6. T. L. Troy, D. L. Page, and E. M. Sevick-Muraca, "Optical properties of normal and diseased breast tissues: prognosis for optical mammography," *J. Biomed. Opt.* **1**(3), 342–355 (1996).
7. I. Georgakoudi et al., "Fluorescence, reflectance, and light-scattering spectroscopy for evaluating dysplasia in patients with Barrett's esophagus," *Gastroenterology* **120**(7), 1620–1629 (2001).
8. Y. N. Mirabal et al., "Reflectance spectroscopy for in vivo detection of cervical precancer," *J. Biomed. Opt.* **7**(4), 587–594 (2002).
9. A. Garcia-Uribe et al., "Skin cancer detection by spectroscopic oblique-incidence reflectometry: classification and physiological origins," *Appl. Opt.* **43**(13), 2643–2650 (2004).
10. A. Garcia-Uribe et al., "Epithelial cancer detection by oblique-incidence optical spectroscopy," *Proc. SPIE* **7169**, 71690A (2009).
11. W. A. Wells et al., "Phase contrast microscopy analysis of breast tissue: differences in benign vs. malignant epithelium and stroma," *Anal. Quant. Cytol. Histol.* **31**(4), 197–207 (2009).
12. J. W. Pickering et al., "Double integrating-sphere system for measuring the optical properties of tissue," *Appl. Opt.* **32**(4), 399–410 (1993).
13. B. C. Wilson, T. J. Farrell, and M. S. Patterson, "An optical fiber-based diffuse reflectance spectrometer for noninvasive investigation of photodynamic sensitizers in vivo," in *Future Directions and Applications in Photodynamic Therapy*, C. J. Goner, Ed., SPIE Institute Series, Vol. IS06, PIE, Bellingham (1990).
14. S. L. Jacques et al., "Video reflectometry to extract optical properties of tissue in vivo," in *Medical Optical Tomography: Functional Imaging and Monitoring*, SPIE Institute Series, Vol. IS11, SPIE, Bellingham (1993).
15. L. Wang and S. L. Jacques, "Use of a laser beam with an oblique angle of incidence to measure the reduced scattering coefficient of a turbid medium," *Appl. Opt.* **34**(13), 2362–2366 (1995).
16. S. P. Lin et al., "Measurement of tissue optical properties by the use of oblique-incidence fiber reflectometry," *Appl. Opt.* **36**(1), 136–143 (1997).
17. G. Marquez and L. V. Wang, "White light oblique incidence reflectometer for measuring absorption and reduced scattering spectra of tissue-like turbid media," *Opt. Express* **1**(13), 454–460 (1997).
18. A. Garcia-Uribe et al., "High-transmission-efficiency and side-viewing micro OIDRS probe for fast and minimally invasive tumor margin detection," *IEEE Sens. J.* **11**(4), 891–896 (2011).
19. A. Garcia-Uribe et al., "In vivo diagnosis of melanoma and nonmelanoma skin cancer using oblique incidence diffuse reflectance spectrometry," *Cancer Res.* **72**(11), 2738–2745 (2012).
20. M. D. Risi, A. R. Rouse, and A. F. Gmitro, "Fused oblique incidence reflectometry and confocal fluorescence microscopy," *Proc. SPIE* **7893**, 78930F (2011).
21. J. Yi and V. Backman, "Imaging a full set of optical scattering properties of biological tissue by inverse spectroscopic optical coherence tomography," *Opt. Lett.* **37**(21), 4443–4445 (2012).
22. L. Thrane et al., "Extraction of tissue optical properties from optical coherence tomography images for diagnostic purposes," *Proc. SPIE* **5771**, 139–150 (2005).
23. R. Leitgeib et al., "Spectral measurement of absorption by spectroscopic frequency-domain optical coherence tomography," *Opt. Lett.* **25**(11), 820–822 (2000).
24. D. J. Faber, F. J. van der Meer, and M. C. G. Aalders, "Quantitative measurement of attenuation coefficients of weakly scattering media using optical coherence tomography," *Opt. Express* **12**(19), 4353–4365 (2004).
25. A. I. Kholodnykh et al., "Precision of measurement of tissue optical properties with optical coherence tomography," *Appl. Opt.* **42**(16), 3027–3037 (2003).
26. J. M. Schmitt, A. Knuettel, and R. F. Bonner, "Measurement of optical properties of biological tissues by low-coherence reflectometry," *Appl. Opt.* **32**(30), 6032–6042 (1993).
27. K. Johnson et al., "Elastic scattering spectroscopy for intraoperative determination of sentinel lymph node status in the breast," *J. Biomed. Opt.* **9**(6), 1122–1128 (2004).
28. I. J. Bigio et al., "Diagnosis of breast cancer using elastic-scattering spectroscopy: preliminary clinical results," *J. Biomed Opt.* **5**(2), 221–228 (2000).
29. W. A. Wells et al., "Phase contrast microscopy analysis of breast tissue; differences in benign vs. malignant epithelium and stroma," *Anal. Quant. Cytol. Histol.* **31**(4), 197–207 (2009).
30. A. H. Hielscher et al., "Near-infrared diffuse optical tomography," *Dis. Markers* **18**(5–6), 313–337 (2002).
31. D. J. Cuccia et al., "Modulated imaging: quantitative analysis and tomography of turbid media in the spatial-frequency domain," *Opt. Lett.* **30**(11), 1354–1356 (2005).
32. Q. Wang et al., "Measurement of internal tissue optical properties at ultraviolet and visible wavelengths: development and implementation of a fiberoptic-based system," *Opt. Express* **16**(12), 8685–8703 (2008).
33. B. Yu et al., "Diffuse reflectance spectroscopy with a self-calibrating fiber optic probe," *Opt. Lett.* **33**(16), 1783–1785 (2008).
34. E. L. Hull and T. H. Foster, "Steady-state reflectance spectroscopy in the P3 approximation," *J. Opt. Soc. Am. A* **18**(3), 584–599 (2001).
35. C. J. deLima et al., "Side-viewing fiberoptic catheter for biospectroscopy applications," *Lasers Med. Sci.* **19**(1), 15–20 (2004).
36. T. J. Farrell and M. S. Patterson, "A diffusion theory model of spatially resolved, steady-state diffuse reflectance for the noninvasive determination of tissue optical properties in vivo," *Med. Phys.* **19**(4), 879–888 (1992).
37. L. Wang et al., "Oblique-incidence reflectometry: one relative profile measurement of diffuse reflectance yields two optical parameters," *Proc. SPIE* **2627**, 165–175 (1995).
38. R. A. Wall and J. K. Barton, "Fluorescence-based surface magnifying chromoendoscopy and optical coherence tomography endoscope," *J. Biomed. Opt.* **17**(8), 086003 (2012).
39. H. Ao et al., "Thermal coagulation-induced changes of the optical properties of normal and adenomatous human colon tissue in vitro in the spectral range 400–1100 nm," *Phys. Med. Biol.* **53**(8), 2197–2206 (2008).
40. D. Hidovic-Rowe and E. Claridge, "Modelling and validation of spectral reflectance for colon," *Phys. Med. Biol.* **50**(6), 1071–1093 (2005).
41. H. Wei et al., "Differences in optical properties between healthy and pathological human colon tissues using a Ti:sapphire laser: an in vitro study using the Monte Carlo inversion technique," *J. Biomed. Opt.* **10**(4), 044022 (2005).
42. G. I. Zoinos et al., "Morphological model of human colon tissue fluorescence," *IEEE Trans. Biomed. Eng.* **43**(2), 113–122 (1996).
43. R. Marchesini et al., "Ex vivo optical properties of human colon tissue," *Lasers Surg. Med.* **15**(4), 351–357 (1994).
44. S. Prahl, "Mie Scattering Calculator," http://omlc.ogi.edu/calc/mie_calc.html (May 2013).
45. J. Han, J. Lee, and J. U. Kang, "Pixelation effect removal from fiber bundle based optical coherence tomography imaging," *Opt. Express* **18**(7), 7427–7439 (2010).
46. D. Arifler et al., "Reflectance spectroscopy for diagnosis of epithelial precancer: model-based analysis of fiber-optic probe designs to resolve spectral information from epithelium and stroma," *Appl. Opt.* **44**(20), 4291–4305 (2005).

Biographies of the authors are not available.